



OPEN Ternary atomized Hollow carbon spheres for high-performance symmetric supercapacitors

Sai Prem Shaji^{1,2}, Mohanraj Madeshwaran^{1,2} & Ulaganathan Mani^{1,2}✉

Hollow carbon spheres are among the most promising materials for supercapacitor electrodes. Here, N, S, and F-doped hollow carbon spheres have been synthesized, and their electric double layer supercapacitor (EDLC) performances have been investigated in a KOH electrolyte. It is found that the device with electrodes having N, S, and F ternary atom-doped material delivers superior performance and rate capability compared to N-doped and N, S co-doped materials. The ternary atom-doped device delivered a specific energy of 11.15 Wh kg⁻¹ at a power density of 208 W kg⁻¹. The EDL symmetric capacitor delivered 6.83 Wh kg⁻¹ even at a higher specific power of 10 kW kg⁻¹ (5 A g⁻¹). The EDL symmetric capacitor exhibited excellent capacitance retention of 89% and a coulombic efficiency of 100% after 22,000 cycles at 1 A g⁻¹. Thus, the ternary atom-doped material emerges as a better candidate for versatile and high-performance devices in a wide range of high-energy, high-power applications.

Keywords Supercapacitor, EDLC, Hollow carbon sphere, Aqueous electrolyte, Ternary atom doping

Supercapacitors are of great significance due to their higher specific power ratings and good cycle life^{1–3}. Among various types of supercapacitors, electric double-layer capacitors (EDLCs) are the simplest yet most significant and commonly used⁴. Supercapacitors (SCs) are utilized in various applications, including instantaneous electricity compensators, memory backup systems, auxiliary power units, and other systems that store energy⁵. In addition, SCs have potential applications in hybrid electric vehicles⁶. The non-faradaic charge storage mechanism of the carbonaceous materials provides high power. As a result, these materials have been employed as positive or negative electrodes in hybrid devices where the carbon electrodes determine the rate capability and power of the devices. EDLCs achieve charge storage through the physical adsorption and desorption of charges on the surface of the capacitor device's electrodes during the charge and discharge processes, respectively, which is a purely surface phenomenon. Charges are stored by rapidly creating double layers of charges at the electrode-electrolyte interface⁶. Mostly, carbonaceous materials have been employed as EDLC electrode materials due to their good electrochemical active surface area, pore volumes, and good chemical and electrochemical stability⁷. Hollow carbon spheres are spheres of carbon with a void inside them. The walls of the hollow spheres are often porous. These properties provide them with good mechanical strength, high surface area, and low specific density⁸. As no chemical reactions occur at the surface of an EDLC device, the performance of an EDLC device largely depends on the physical properties of the materials used as electrodes, which include surface area, porosity, wettability, and electrical conductivity. To improve the conductivity of carbonaceous materials, a common practice is to dope them with suitable impurities. Many studies have shown that doping with electronegative atoms, such as nitrogen, sulfur, and fluorine, can significantly enhance the electronic conductivity of the electrode, thereby improving the electrochemical performance of the device^{5,9}. Incorporating F and S can also improve the wettability of the hollow carbon spheres. Sulfur can form polar functional groups, such as C-S and C-SOx, which increase surface polarity and improve surface interaction with the electrolyte. Likewise, the incorporation of F into the carbon matrix can lead to the formation of a C-F bond, which is also polar. The presence of these dopants thus increases the surface energy of the material. The increase in surface energy associated with F and S doping can enhance the wettability of the electrode materials, thereby improving the interaction with the electrolyte^{5,10}. To further improve the performance of EDLC, porosity is usually introduced. The hollow carbon spheres have porous walls that can enhance the electrochemical performance of the device by improving the rate of ion adsorption and desorption at the electrode⁸. Hollow carbon spheres have been synthesized using various approaches. Among them, template-based techniques have been widely employed for the synthesis of HCSs due to their enhanced

¹Department of Physics, Amrita School of Physical Sciences Coimbatore, Amrita Vishwa Vidyapeetham, Coimbatore 641 112, India. ²Functional Materials Laboratory, Amrita School of Engineering Coimbatore, Amrita Vishwa Vidyapeetham, Coimbatore 641 112, India. ✉email: m_ulaganathan@cb.amrita.edu; nathanphysics@gmail.com

pore structure and sphere wall thickness. The porous nature of the samples enables them to be utilized in a wide range of applications. Due to their controlled size and porous nature, HCSs have been used as electrocatalysts in HER¹¹, OER¹², fuel cells¹³, electrode catalysts for gas sensing¹⁴, supercapacitors¹⁵, and Li-ion and Na-ion batteries¹⁶. Due to their effective active surface area and porous nature, HCSs have been successfully utilized in supercapacitors. However, due to their poor conductivity, these HCSs exhibit a limited power-delivering ability. This power-delivering ability of the carbon materials is restricted due to the poor conductivity of the samples. To improve the conductivity of the samples, heteroatoms are doped into the HCSs. Wei Sun et al.¹⁷ studied the effects of compressive stress on the charge storage performance of the symmetric capacitors. Xylose-derived activated carbon spheres have been investigated using the Na₂SO₄ electrolyte at various concentrations. It was observed that the increase of compressive stress from 2.55 to 40.75 MPa decreased the IR drop of the cell from 0.18 to 0.04 V. However, the energy and power relations have not been obtained from this study. Yan Lv et al.¹⁵ prepared N and S co-doped porous carbon spheres using the ultrasonic spray pyrolysis process. The charge storage performance of the carbon spheres has been investigated using the 6 M KOH electrolyte, and the cell delivered 308 F g⁻¹ at 1 A g⁻¹. Further, the cycle life of the SCs was recorded up to 10,000 cycles with a capacitance retention of 90% at 5 A g⁻¹. However, the symmetric device was tested at a potential window of -1 V to -0.1 V, surprisingly. Porous carbon spheres have been investigated using Water-in-Salt Electrolyte (WISE) with a voltage window of 2.6 V. The symmetric capacitor in the WISE electrolyte delivered an energy density of 31.0 Wh kg⁻¹ at 2.4 kW kg⁻¹¹⁸. In this work, we have synthesized Nitrogen doped, Nitrogen (N) and Sulfur (S) co-doped (NS_C) and N, S, and Fluorine co-doped (NFS) doped HCSs. The as-prepared HCSs have been used as electrodes in symmetric supercapacitors. The charge storage performances have been evaluated using cyclic voltammetry (CV), galvanostatic charge-discharge (GCD), and electrochemical impedance spectroscopy (EIS) analysis, which have also been conducted under various conditions. Before the electrode fabrication process, all the prepared materials were subjected to various physical characterizations, including X-ray diffraction, Raman spectroscopy, and X-ray photoelectron spectroscopy (XPS), to ensure the structural behavior and elemental compositions of the materials. Furthermore, the electrochemically high-performing electrode materials were subjected to Transmission Electron Microscopy (TEM) analysis to investigate the structural characteristics of the electrode.

Experimental section

Materials

All materials were used as received. Ammonia-NH₃ (30%) and Dopamine hydrochloride-C₈H₁₁NO₂, HCl (98%) were procured from Sisco Research Laboratories Pvt Ltd (SRL, India), Tetraethyl orthosilicate-Si(OC₂H₅)₄ (98%), and Thiourea SC(NH₂)₂ were obtained from Avra Synthesis Pvt. Ltd, India. Ammonium Fluoride- NH₄F was purchased from Rankem chemicals, and Sodium hydroxide- NaOH was procured from S D Fine-Chem Ltd (SDFCL, India).

Synthesis of heteroatoms doped Hollow carbon spheres

To synthesize nitrogen-doped hollow carbon spheres, 12 mL of ethanol was added to 40 mL of double-distilled water under constant stirring. To the above solution, 0.5 mL ammonia solution was added, and the solution was stirred for 1 h at room temperature. Following this, 0.5 mL of tetraethyl orthosilicate was added, and the solution was stirred for 2 h to form silica spheres. To this, 0.4 g of dopamine hydrochloride was added after dissolving it in 4 mL of DI water, and the mixture was left for polymerization under mild stirring for 48 h at 25 °C. The obtained product was washed and separated by centrifugation using DI water and ethanol, and the resulting sediments were dried at 80 °C for 24 h. At a ramp rate of 30 °C min⁻¹, the obtained polydopamine-silica product was carbonized at 900 °C for 4 h in an Ar atmosphere. This gives Silica/N-doped carbon. This product is treated with 2 M NaOH solution for 48 h to etch out silica impurities. The sample was further washed and dried at 80 °C for 12 h to obtain the final product N-doped hollow carbon sphere (N_C)¹⁹. To synthesize the N and S co-doped sample (NS_C), 1 g of Thiourea was added before the polymerization step. For N, F, and S-doped samples, 0.5 g of ammonium fluoride and 0.5 g of Thiourea were added immediately before the polymerization step, where ammonium fluoride serves as an F source.

Three-electrode testing analysis

Before the symmetric capacitor fabrication and testing analysis, all the electrodes were subjected to three-electrode analysis to understand the potential window of the electrodes. The electrodes have been prepared using the as-prepared materials with acetylene black and Polyvinylidene fluoride (PVDF) at a ratio of 85:10:05 wt%. The slurry was prepared using N-methyl-2-pyrrolidone to dissolve the PVDF, and the obtained homogenous slurry was coated on the given Ni-foam. The mass loading on the as-prepared electrodes was measured and it was in the range of 3–3.5 mg. The as-prepared electrode, Pt wire, and standard calomel electrodes were used as the working, counter, and reference electrodes, respectively. All the electrodes in a three-electrode system were tested in 2 M KOH electrolyte.

Symmetric capacitor fabrication

To prepare the electrodes, active material (N_C/NS_C/NFS_C), acetylene black, and PVDF were mixed in a ratio of 85:10:5 and then ground together. To this mixture, an appropriate volume of NMP solvent was added, and the mixture was ground well until a homogeneous slurry was obtained. The slurry was coated onto Ni foam cut into a circular shape, resulting in approximately 3 to 3.25 mg of loading on each electrode. Before the coating, Ni-foam was crunched into a thin sheet. The electrodes were then dried at 60 °C for 12 h. Thus, symmetric CR2032 coin-type capacitors (AC||KOH||AC) were fabricated using a hydraulic coin cell crimping machine, where the as-prepared electrodes served as the active electrodes by placing a separator between them, and 2 M KOH was

employed as the electrolyte. Symmetric supercapacitors (SCs) were fabricated for all three samples, including N-doped HCS, N and S co-doped HCS, and N, S, and F co-doped HCS. The capacitors were named N-SC, NS-SC, and NFS-SC, respectively. Furthermore, the as-fabricated symmetric capacitors were subjected to various electrochemical characterizations, including GCD, CV, and EIS. All the electrochemical characterizations were recorded using Origaly's France (Origaflex 1 A-OGFEIS) electrochemical workstation.

Physical characterization

To understand and analyse the physical properties of the as-prepared samples, they were subjected to various physical characterization techniques such as X-ray diffraction (XRD), Raman Spectroscopy, Brunauer–Emmett–Teller (BET) analysis, X-ray Photoelectron Spectroscopy (XPS), Field emission scanning electron microscopy (FESEM) and Transmission electron microscopy (TEM). A Bruker D8 diffractometer with Cu-K α radiation ($\lambda = 1.5418 \text{ \AA}$) was used to record the XRD pattern of the samples over a 2θ range of $10\text{--}90^\circ$ at a scan rate of 3° per minute. A Renishaw confocal Raman microscope, utilizing a 532 nm laser source, was employed to record the Raman spectra of the as-prepared samples. The surface morphology of the samples was analysed and studied using a Carl Zeiss SUPRA 55VP model Field Emission Scanning Electron Microscope (FESEM), and to analyse more intricate details of the surface and structure, a High Resolution-Transmission Electron Microscope (HR-TEM, JEOL, Japan (JEM-2100 plus)) was used. To understand the wettability behavior of the synthesized compound, contact angle measurements were carried out using a Crus-DSA30 meter. To study the porous nature and surface area that the samples can provide, a Quantachrome ASiQwin automated gas sorption data acquisition and reduction analyzer was used to conduct a BET analysis. A Thermo Scientific MultiLab-2000 X-ray Photoelectron Spectrometer was used to study the chemical composition of the samples.

Results and discussion

All the prepared samples were subjected to X-ray diffraction (XRD) analysis, and the obtained XRD patterns are shown in Fig. 1a. There are two characteristic peaks of carbonaceous materials that can be seen in the XRD pattern. The first and most prominent peak is at the 2θ value of 25° , corresponding to the (002) graphitic plane, and the second peak at 43.6° corresponds to the (100) characteristic plane of carbonaceous materials. The broad nature of the above characteristic peaks obtained here indicates the amorphous nature of the HCS samples. In comparison with the N_C sample, the NS_C and NFS_C samples exhibit slightly sharper peaks at 25° , which may be attributed to the increased graphitic nature of these samples, as also evidenced by the Raman spectral analysis.

Further, the enhanced graphitic nature of the samples can improve the stability under severe operating conditions and over a large number of cycles^{20,21}. The amorphous nature of the materials makes them suitable for EDLC-type supercapacitor applications due to their high surface area and possible porous nature^{22,23}. This is also evidenced by the CV and GCD studies of the sample. Raman spectra (Fig. 1b) showed the two characteristic peaks at 1356 and 1595 cm^{-1} , corresponding to the D band and G band of the carbon materials. The D band, also known as the disorder or defect band, indicates the presence of disorder, defects, doping, or non- sp^2 hybridized carbon sites. In contrast, the G band indicates the graphitic nature of the carbon material. It corresponds to the E_{2g} vibrations of sp^2 -bonded carbon atoms in the sample. This vibrational mode involves the stretching of C–C bonds within the graphitic plane²⁴. As the percentage of the sp^2 graphitic content in the sample increases, the intensity of the G band also increases. The ratio of intensities of these peaks, I_D/I_G , is a crucial parameter in the Raman spectrum of a carbonaceous material. It helps to evaluate the degree of disorder or the extent of non- sp^2 sites in the sample^{23,25}. The I_D/I_G ratios of N_C, NS_C, and NFS_C samples are 0.882, 0.958, and 0.962, respectively. The higher values of the I_D/I_G ratio of NS_C and NFS_C indicate that these samples have more disorder associated with them. This could be directly attributed to the presence of multiple dopants in the material. Surface area and pore volume are two factors that significantly affect the performance of an EDLC supercapacitor. To understand these characteristics of the prepared carbon samples, BET analysis was carried out, and the obtained N_2 adsorption and desorption isotherms of the samples are shown in Fig. 1c. All three samples showed a similar type of hysteresis loop. It was observed that at lower relative pressure, the samples exhibited a steep increase in the volume of adsorbed N_2 , indicating strong adsorption of the gas molecules by the carbon materials. This is indicative of the microporous or lower mesoporous nature of the material. In the mid region, the isotherms show a gradual increase in the adsorbed volume, signifying the multilayer adsorption on the surface and mesopore filling. At the high relative pressure region, there is again a sharp increase in the adsorption, indicating the capillary condensation within the mesopores. This phenomenon occurs when gas condenses in the pore at a pressure lower than the saturation pressure (P_0) of the bulk fluid²⁶. Now, upon reduction of pressure from the peak point, the gas molecules begin to desorb from the surface of the material. During this process, the isotherm follows a different path, giving rise to a hysteresis loop. The shape of the adsorption/desorption isotherm and the hysteresis loop suggest that all samples follow the type IV isotherm. The specific BET surface areas calculated for the samples were 579.08, 324.20, and $108.39 \text{ m}^2/\text{g}$ for N_C, NS_C, and NFS_C, respectively. The reduction in the surface area of the co-doped and ternary doped samples NS_C and NFS_C could be attributed to the fact that doping can, at times, block the active sites of the carbon, reducing the active surface area available for adsorption^{27–29}. Figure 1d presents the pore size distribution curves of the N_C, NS_C, and NFS_C samples, providing detailed insights into the contribution of different pore sizes to the overall pore volume. The N_C sample exhibits a sharp and intense peak in the range of $10\text{--}20 \text{ \AA}$, indicative of a high concentration of narrow micropores. In contrast, the NS_C sample displays peaks of notably lower intensity within the same range, suggesting partial blockage or suppression of micropore formation due to sulfur doping. The NFS_C sample exhibits broader peaks extending from approximately 10 to 40 \AA , indicating a wider pore distribution and suggesting the presence of larger mesopores. This broadening is attributed to the synergistic effect of sulfur and fluorine co-doping, which appears to induce micropore blocking and structural etching,

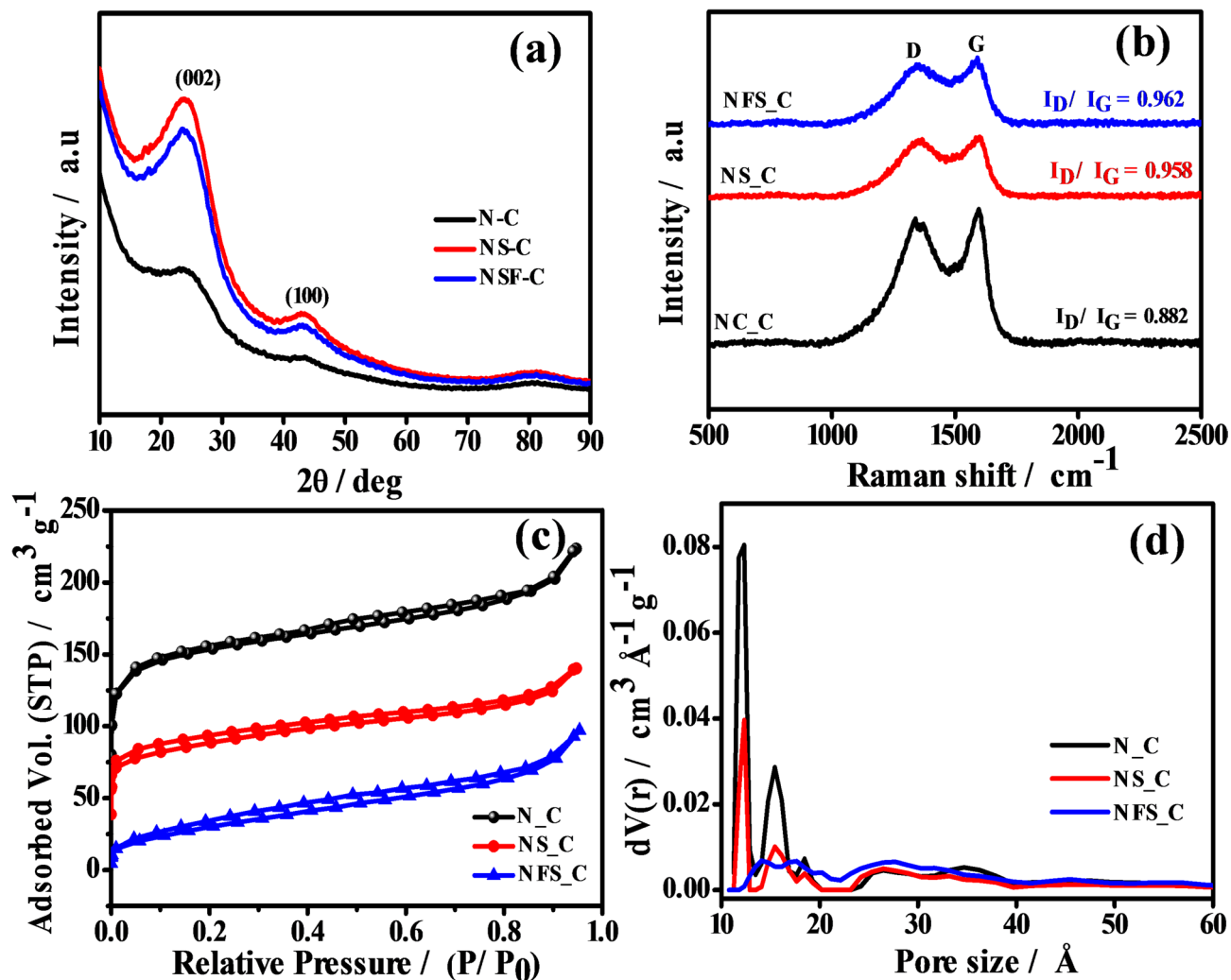


Fig. 1. **a** XRD pattern of the samples. **b** Raman spectra of the samples. **c** BET isotherms of the samples. **d** Pore size distribution of the as prepared samples under this study.

leading to pore enlargement and, in turn, reducing the total surface area. Nevertheless, for supercapacitor applications, these dopants significantly enhance wettability and conductivity, which are two other crucial factors that can help improve the performance of supercapacitors. The heteroatom doping also enhances the device's stability over a large number of charging and discharging cycles^{30–32}. The improved wettability of the samples has been demonstrated by contact angle measurements using a 2 M KOH electrolyte. The obtained photographic image of the droplets is shown in Fig. S1. The measurement was carried out for 30 s, clearly showing that the surface adsorption characteristics of the NSF_C electrode are better than those of the N_C and NS_C electrodes.

To understand the chemical nature of the samples, they underwent XPS analysis. Figure S2a–c presents the XPS survey spectrum of the N_C, NS_C, and NFS_C samples, respectively. The dominant C-1s peak indicates a carbon-rich structure. The survey spectrum supports the successful incorporation of heteroatoms in the carbon matrix. To understand the chemical bonding in the sample, the obtained spectra were further deconvoluted and analysed. Figure 2a–c shows the deconvoluted XPS C-1s spectra for the N_C, NS_C, and NFS_C samples. There are three major peaks in the deconvoluted C-1s spectra. The most intense peak at 284.4 eV is associated with graphitic carbon (C=C). The peaks at 285.5 eV and 288.5 eV are broader, suggesting a contribution from heteroatom doping. The peak at 285.5 eV is associated with the C–N bond, while the broader peak around 288.5 eV is attributed to C–F and N–C=O bonds within the carbon structure. Figure 2d–f shows the high-resolution XPS N-1s spectra of the N_C, NS_C, and NFS_C samples. There are three peaks in the deconvoluted N-1s spectra. They correspond to the different configurations of nitrogen-carbon bonds, namely pyridinic, pyrrolic, and graphitic nitrogen. The peak at 398 eV is associated with the pyridinic nitrogen. The peaks at 400 and 403 eV correspond to pyrrolic and graphitic nitrogen, respectively. The presence of these nitrogen configurations can enhance the electronic properties and improve conductivity. The graphitic nitrogen will also increase the stability of the structure. Figure 2g, h shows the deconvoluted spectra of S 2P for the NS_C and NFS_C samples. Two prominent peaks are observed at 163.5 eV and 167.4 eV, corresponding to different sulfur species within the carbon structure. The peak at 163.5 eV corresponds to the C–S species, and the peak at 167.4

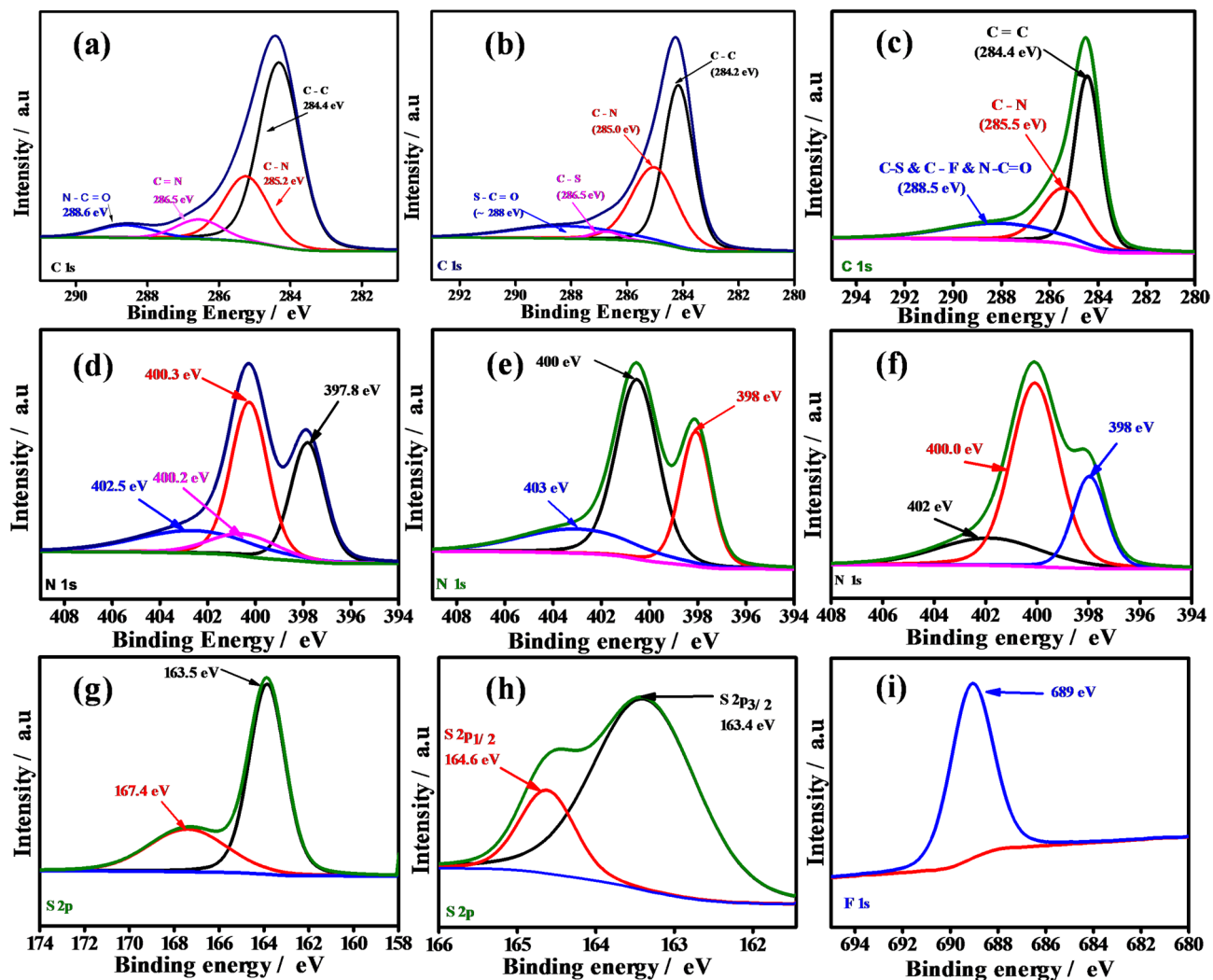


Fig. 2. Deconvoluted XPS spectra of N_C, NS_C, and NSF_C samples. **a–c** C1s spectra of N_C, NS_C, NSF_C samples; **d–f** N1s spectra of N_C, NS_C, NSF_C samples; **g, h** S 2P spectra of NS_C, NSF_C samples; **i** F 1s spectra of NSF_C sample.

is associated with SO_4^{2-} species³³. The XPS results confirm the doping of N, S, and F in the hollow carbon sphere. The presence of S in the C–S form can increase the polarity of the HCS. The polar C–F bonds can also contribute to this. The improved surface polarity can enhance the interaction between the electrode and the electrolyte. This ensures unhindered electrolyte infiltration on the electrode. Allowing even the limited available surface to be fully utilized. Doping with Fluorine can also enhance the structural stability of the carbon material and improve its electron transport ability³⁴. Figure 2i shows the high-resolution XPS F-1s spectra for the ternary atom-doped NFS-C sample. The XPS peak at 689 eV is associated with the C–F bond. The presence of Fluorine can considerably increase the conductivity and wettability of the HCS.

To confirm the hollow and spherical surface morphology of the as-prepared samples, all the samples were subjected to FESEM analysis. Figure 3 shows the surface images obtained at different magnifications of the nitrogen-doped (Fig. 3a–c), nitrogen-sulfur co-doped (Fig. 3d–f), and nitrogen-fluorine-sulfur co-doped (Fig. 3g–i) HCSs. From the FESEM images, it is evident that the samples exhibit a spherical morphology. It can also be observed that the spheres are closely packed microspheres with sizes ranging from 300 to 400 nm. The microspheres are hollow, with walls that have a porous structure. Several broken spheres reveal the hollow nature of the carbon spheres. These broken shells are formed due to thermal stress at some of the weak walls of the spheres. The spherical morphology enhances the surface-to-volume ratio, and hence, it is expected to provide a high surface area, which can improve the charge storage performance of the supercapacitors. Thus, the hollow spherical morphology, combined with porous walls, makes them a highly suitable set of materials for supercapacitor applications^{35,36}.

Elemental mapping was performed on the NFS_C sample to confirm the incorporation and spatial distribution of dopant elements within the carbon matrix. Figure 4a shows the combined elemental mapping of C, O, S, N, and F in the sample. Individual mapping of the elements is shown in Fig. 4b–f for the elements C, O,

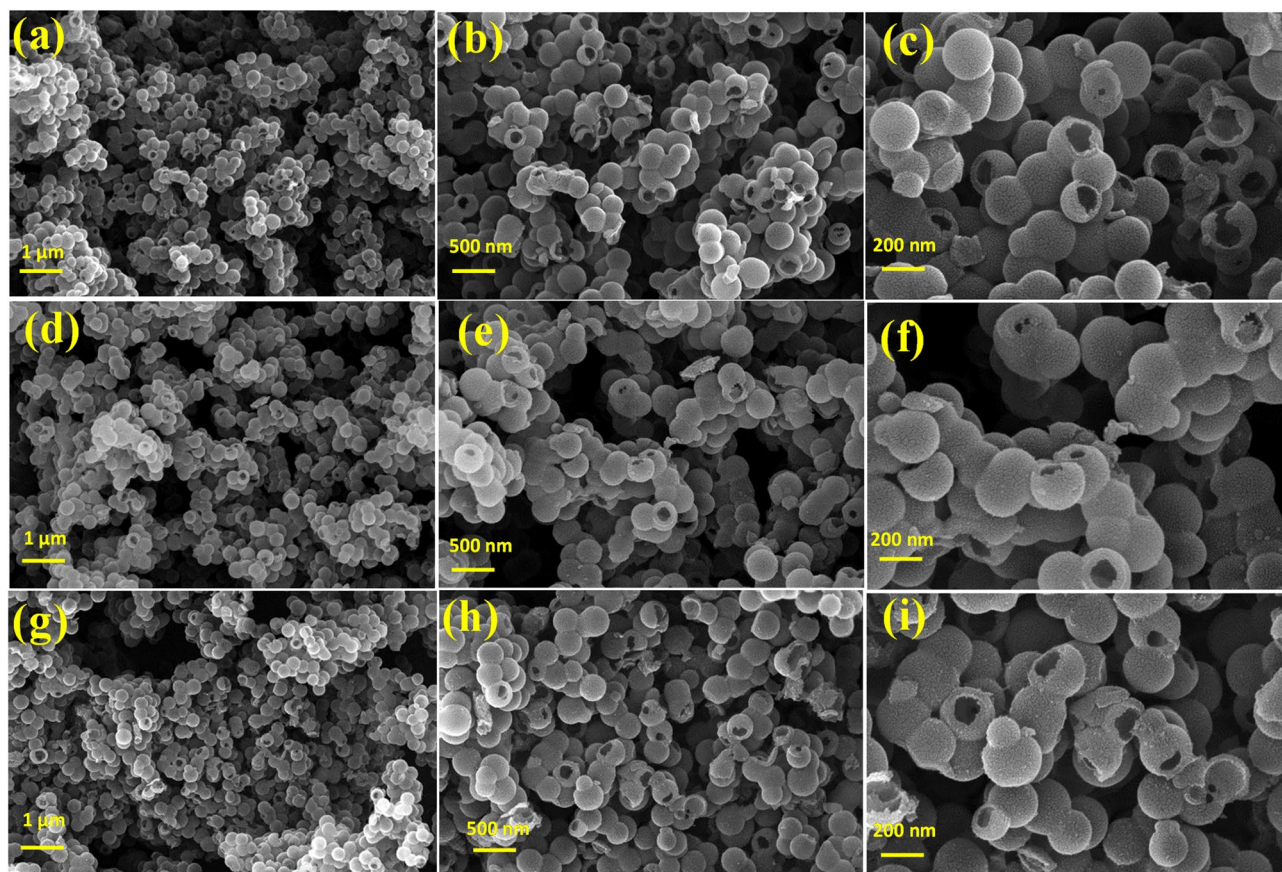


Fig. 3. a–c FESEM images of N_C sample at different magnifications. d–f FESEM images of NS_C sample at different magnifications. g–i FESEM images of NFS_C sample at different magnifications.

S, N, and F, respectively. The above images confirm the presence of N, S, and F in the NFS sample. The images also suggest the uniform distribution of these elements in the sample.

Figure 5a–c shows the high-resolution TEM images of the NFS_C sample, indicating the disordered arrangement and the amorphous nature of the material. The surface appears to be porous, exhibiting non-uniform porosity. The selected area electron diffraction (SAED) pattern presented in Fig. 5d shows diffused rings. The rings are distinct but not well-defined, indicating the amorphous nature of the material. The diffused nature of the rings and the absence of bright spots in the SAED pattern confirm the lack of long-range order, and the obtained results are well consistent with the existing HCSs^{37,38}.

Electrochemical characterizations

Half cell analysis of N_C, NS_C, NSF_C electrodes

Figure 6a shows the normalised CV comparison of N_C, NS_C, and NSF_C electrodes at 20 mV s⁻¹ scan rate recorded at 0 to -1 V; From the CV curve, it is observed that NFS_C-based samples show improved current density compared to the other electrode materials, indicating the improved electrochemical activity of the samples. The enhanced activity may be attributed to the incorporation of the F in addition to the N, S atoms. Figure 6b shows the GCD comparison of N_C, NS_C, and NSF_C electrodes at a current density of merely 1.7 A g⁻¹; the discharge time for the NSF_C electrode is better than that of the remaining electrodes. Figure 6c EIS comparison of N_C, NS_C, and NSF_C electrodes at the frequency ranging from 100 kHz to 100 mHz; the electrodes deliver the equivalent charge transfer resistance of 17, 7.5, and 6 Ω for N_C, NS_C, and NSF_C electrodes, respectively. Figure 6d–f shows the cyclic voltammetry of the N_C, NS_C, and NSF_C electrodes obtained at various scan rates of 10 to 100 mV s⁻¹ at a step of 10 mV s⁻¹. All samples showing quasi-rectangular CV curves and their shapes have been retained, even at 100 mV s⁻¹. Furthermore, the current density of the curves increases with the increase in scan rate, and the shape of the CV curves is slightly altered, which may be attributed to increased polarization at the electrode surfaces. Figure 6g shows the GCD curves corresponding to the N_C, recorded at 1.66, 3.33, 5, 6.66, 8.33, and 10 A g⁻¹. GCD curves recorded for the NS_C and NFS_C at different current ranges are shown in Fig. 6h and i. From the obtained GCD profiles, the calculated specific capacitances are 46.43, 32, 21.8, 13.33, 7.75, and 2.68 F g⁻¹ for N_C; and 37.05, 33.06, 29.1, 26.22, 23.16, and 20.8 F g⁻¹ for NS_C; and 72.86, 62.06, 52.7, 44.53, 37.66, and 30.5 for NSF_C electrodes, at the current density of 1.66, 3.33, 5, 6.66, 8.33, and 10 A g⁻¹, respectively were obtained, the specific capacitance values calculated for different current densities are compared in Fig. S3.

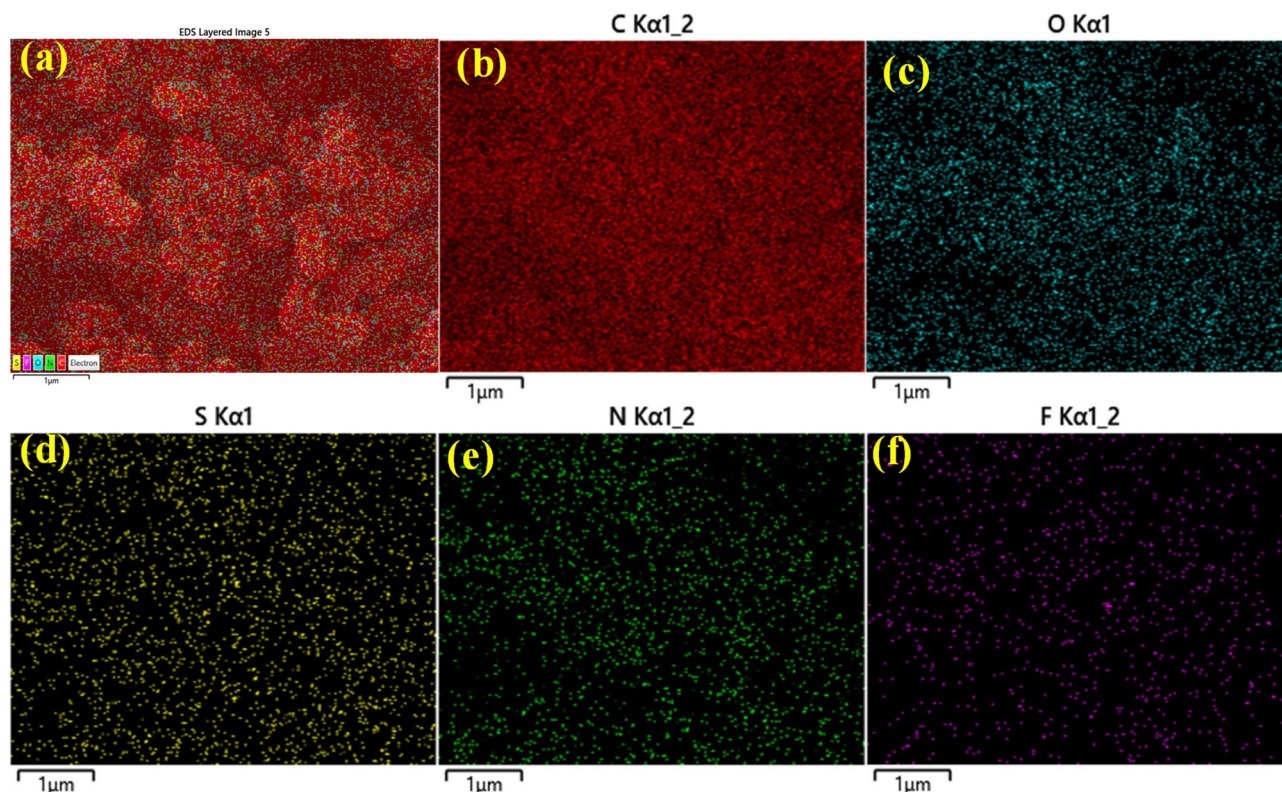


Fig. 4. **a** Elemental mapping of C, O, S, N, and F in the NFS_C sample. **b–f** Individual mapping of C, O, S, N, and F, respectively, in the NFS_C sample.

Symmetric capacitors

Electrochemical characterizations, including CV, GCD, and EIS studies, have been carried out for the Symmetric Capacitors. CV curves of the as-fabricated SCs were recorded at different scan rates and various potential ranges. Figure 7a shows the cyclic voltammogram of the NFS_C device, taken at different voltage windows from 0 to 0.5 V to 0 to 1.1 V at a scan rate of 30 mV s^{-1} . It is essential to operate the supercapacitor device at an optimum voltage window to ensure high efficiency and longer cycle life. Here, it is observed that as the voltage exceeds 1 V, a sharp spike in the current density occurs. This is attributed to the decomposition of the electrolyte. So, the voltage window for all further tests was fixed at 0 to 1 V. Figure 7c–e, shows the cyclic voltammogram of N-C, NS_C, and NFS_C SCs, respectively, recorded at different scan rates ranging from 5 to 100 mV s^{-1} . CVs of the devices under investigation are compared at a scan rate of 30 mV s^{-1} in Fig. 7b. It is observed that the area under the curve for NS_C is lesser when compared to N_C and NFS_C, this could be attributed to the blockage or suppression of micropores on the HCSs by the dopant making the area available for adsorption lesser than N_C device which is confirmed by BET analysis as well. It is also worth noting that NS_C and NFS_C devices exhibit better rectangular curves, which makes them more stable at higher currents and larger numbers of cycles. The area under the curves of N_C and NFS_C are almost the same. This high performance, despite the lower BET surface area, could be attributed to the increased wettability and conductivity of the NFS_C sample due to the presence of F atoms^{5,9}. It could be inferred from the analysis that NFS_C is a better candidate for EDLC devices as it shows better double-layer capacitance behaviour, which is indicated by near-perfect rectangular CV curves. It could be seen that all three CV curves (Fig. 7c–e) show rectangular behaviour, but the NFS_C device is showing more rectangular curves, even at high scan rates. The CV curves, specifically Fig. 7e, exhibit well-defined, symmetric curves, clearly indicating the existence of a double layer at the electrodes. It is worth noting that the current density increases with an increase in scan rate for all three devices, as expected. This could be attributed to a faster rate of reactions occurring at the electrode with an increase in scan rates³⁹. At higher scan rates, a rapid rise in voltage forces more ions to move toward the electrode surface in a shorter period, thereby increasing the current. For all three devices, it is also notable that as the scan rate increases, the curves become increasingly distorted from their ideal rectangular shape. This occurs due to ohmic resistive losses and inadequate time, during which ions get adsorbed and desorbed at the surface, resulting in incomplete charging of the capacitor. Especially in porous material at higher scan rates, ions will not be able to access all pores due to insufficient time to complete the adsorption reactions^{40,41}. Figure 7f shows the variation of specific capacitance with respect to scan rate for all the samples. It is worth noting that, at low scan rates, N_C yields a slightly higher specific capacitance. However, as the scan rate increases, the capacitance value reduces drastically. However, among the three, the NFS_C sample shows the highest particular capacitance across the entire range,

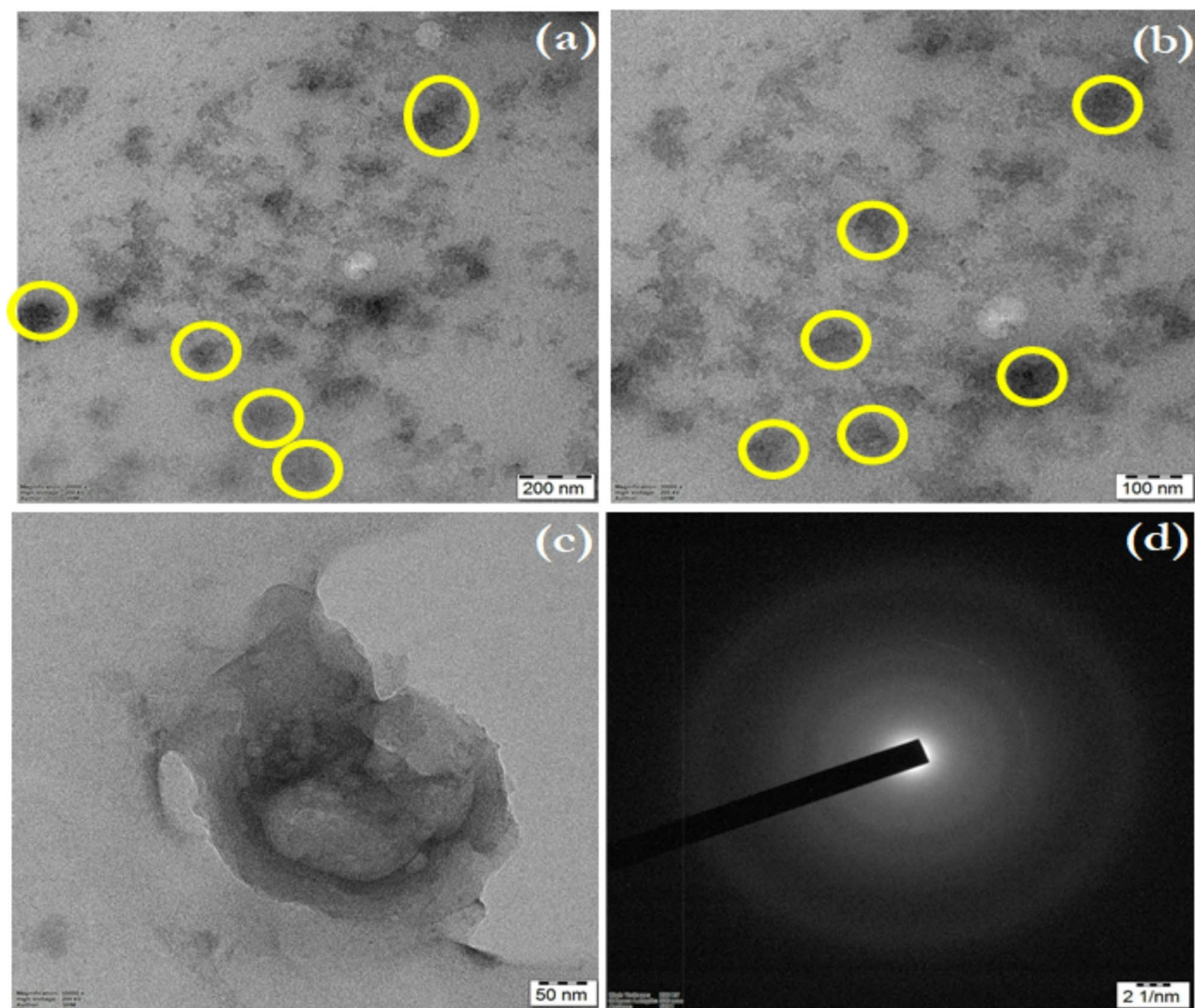


Fig. 5. a–c High-resolution TEM images of the NFS_C sample. d SAED pattern of the NFS_C sample.

highlighting the beneficial synergistic effects of N, S, and F co-doping. Moreover, NFS_C demonstrates superior rate capability, retaining a significant portion of its capacitance at high scan rates.

To elucidate the capacitance performance, the SCs were subjected to GCD analysis, and the GCD curves recorded at different current ranges are shown in the Fig. 8. Figure 8a shows the GCD curves of NFS_C SC tested at various voltage windows for optimizing the potential window. GCD curves of the devices under study are compared in Fig. 8b at 0.25 A g^{-1} . It is worth noting that the devices exhibit triangular GCD curves, indicative of EDLC behavior. However, it is observed that at higher current densities, the curve for the N_C device becomes distorted from its symmetric triangular shape and exhibits an increased IR drop, which is manifested as a sharp voltage drop at the beginning of the discharge curve. IR drop is indicative of the internal resistance of the device due to low conductivity. IR drop in the case of NS_C and NFS_C is very low due to the presence of S and F, S, respectively which increases the conductivity of the electrode. The specific capacitance of the devices is calculated from GCD data using Eq. (1).

$$C_s = \frac{I\Delta t}{m\Delta V} (\text{F g}^{-1}) \quad (1)$$

Where C_s is the specific capacitance, I is the discharge current, Δt is the discharge time, m is the mass loading, and ΔV is the voltage window. Figure 8c–e shows the GCD curves for NFS_C, NS_C, and N_C devices, respectively, obtained at different rated currents. As expected, the curves show that as the applied current increases, the charging and discharging times reduce, and the potential of the SCs increases linearly during the GCD process, indicating that the charge storage phenomenon here is purely a non-faradaic process caused only by physical adsorption/desorption. Figure 8f shows the variation of specific capacitance with increasing current density for N_C, NS_C, and NFS_C devices. Specific capacitance decreases with an increase in current density due to polarization effects at the electrode at high current densities. It can be seen that, although the specific capacitance

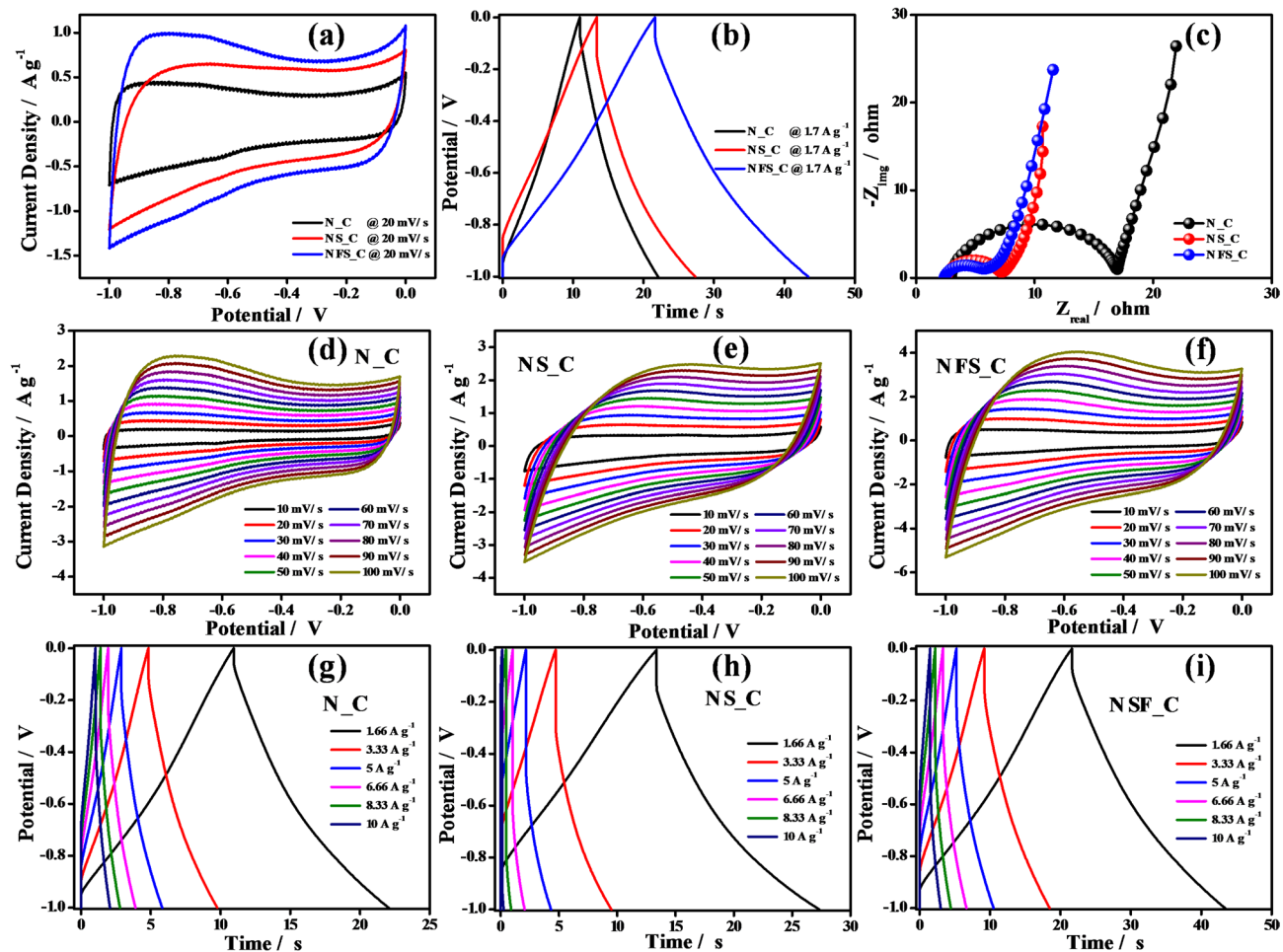


Fig. 6. **a** Electrochemical half-cell analysis: **a** CV comparison of N_C, NS_C, NSF_C electrodes at 20 mV s⁻¹ scan rate. **b** GCD of N_C, NS_C, NSF_C electrodes merely at 1.7 A g⁻¹ current density; **c** EIS comparison of N_C, NS_C, NSF_C electrodes at the frequency ranging from 100 kHz to 100 mHz; **d** CV of N_C electrode at 10–100 mV s⁻¹ scan rates; **e** CV of NS_C electrode at 10–100 mV s⁻¹ scan rates; **f** CV of NSF_C electrode at 10–100 mV s⁻¹ scan rates; **g** GCD of N_C 1.66, 3.33, 5, 6.66, 8.33, and 10 A g⁻¹ current densities. **h** GCD of NS_C at 1.66, 3.33, 5, 6.66, 8.33, and 10 A g⁻¹ current densities. **i** GCD of NSF_C electrode at 1.66, 3.33, 5, 6.66, 8.33, and 10 A g⁻¹ current densities tested at a potential window of -1 to 0 V.

of the N_C device is the highest at low current density, it decreases drastically with an increase in current. At 0.1 A g⁻¹ current density, the N_C device delivers a specific capacitance of 88.8 F g⁻¹, whereas NS_C and NSF_C devices delivered only 59.2 and 80.3 F g⁻¹, respectively. Rate capability is a crucial parameter used to evaluate the performance of any energy storage device. It refers to a device's ability to maintain its performance at varying charging and discharging current rates. It is indicative of a device's ability to operate effectively under various current densities and power demands. It can be observed from Fig. 8f that the ternary atom-doped devices exhibit a higher rate capability. It is noted that the specific capacitance delivered by NS_C at 3.5 A g⁻¹ is 35.9 F g⁻¹, whereas the NSF_C device delivers a specific capacitance of 54 F g⁻¹ at 3.5 A g⁻¹, but N_C delivers only 29.2 F g⁻¹ at the same current density.

A Ragone plot is a graphical representation of specific energy and specific power of various devices, usually plotted on a log scale, which is used to compare the performance of these devices. The specific energy and specific power of N_C, NS_C, and NSF_C devices are given in Fig. 9a. It is observed that the specific energy of the devices decreases as specific power decreases. This trade-off is a characteristic of energy storage devices. The specific energy and specific power of the devices are calculated using the formulae (2) and (3), respectively.

$$E = \frac{1}{2} \cdot \frac{CsV^2}{3.6} \text{ (Wh kg}^{-1}\text{)} \quad (2)$$

$$P = \frac{E}{\Delta t} \times 3600 \text{ (W kg}^{-1}\text{)} \quad (3)$$

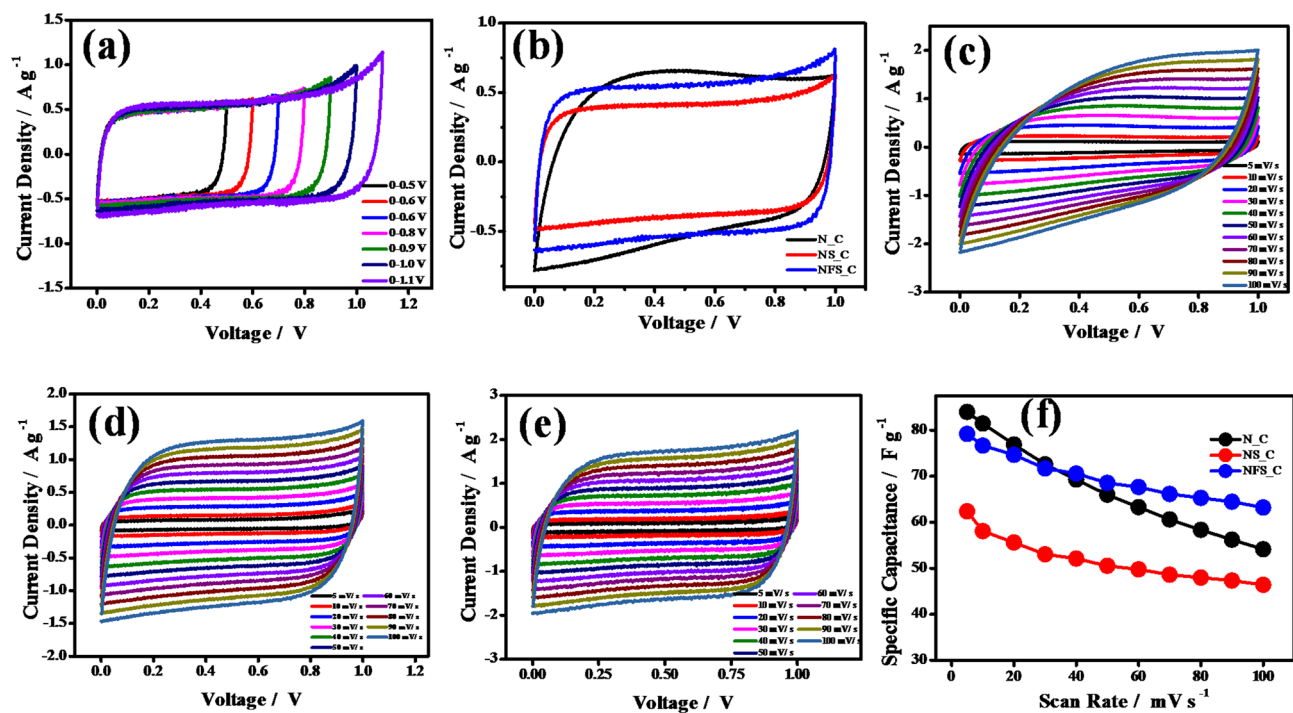


Fig. 7. **a** CV of NFS_C sample at different voltage windows. **b** Comparison of CV of the devices at 30 mV s^{-1} , **c** CV of N_C device at scan rates from 5 mV s^{-1} to 100 mV s^{-1} , **d** CV of NS_C device at scan rates from 5 mV s^{-1} to 100 mV s^{-1} , **e** CV of NFS_C device at scan rates from 5 mV s^{-1} to 100 mV s^{-1} . **f** Comparison of the specific capacitance of the samples at various scan rates.

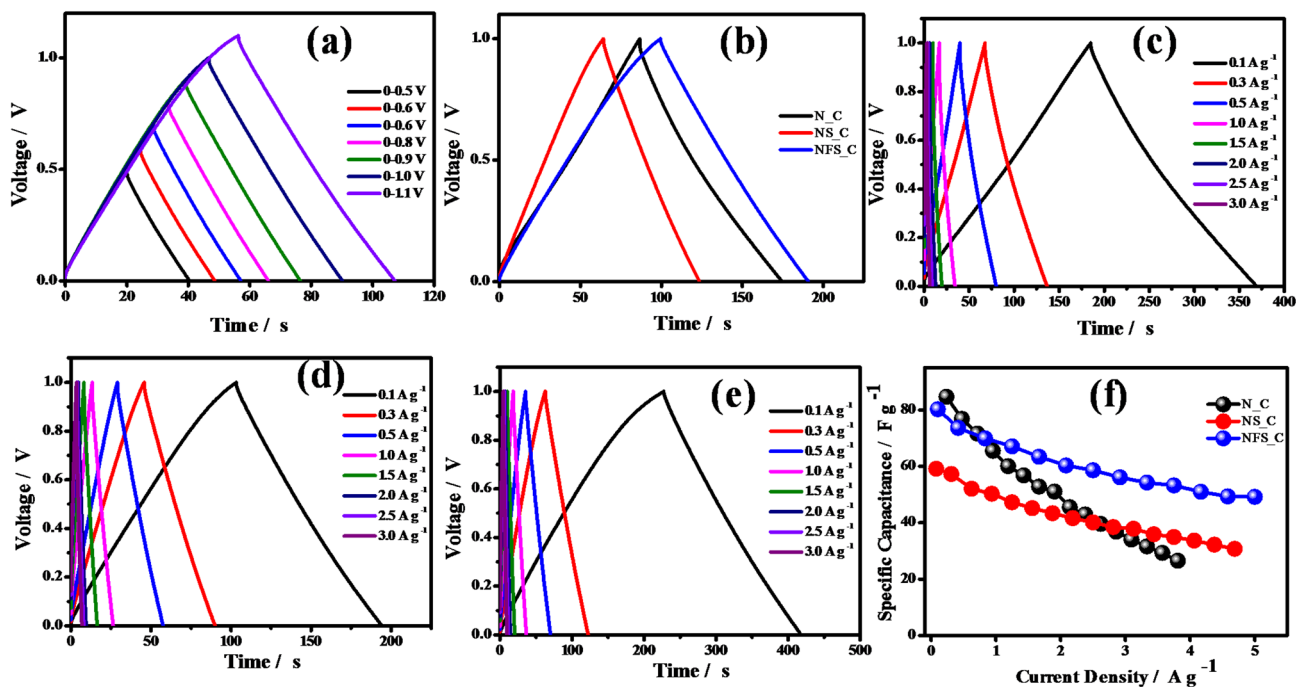


Fig. 8. **a** GCD curves of the NFS_C device at various voltage windows. **b** GCD curves of N_C, NS_C, and NFS_C devices at 0.25 A g^{-1} . **c** GCD curves of the N_C device at various current densities. **d** GCD curves of the NS_C device at various current densities. **e** GCD curves of the NFS_C device at various current densities. **f** Comparison of the specific capacitance of the devices at different current densities.

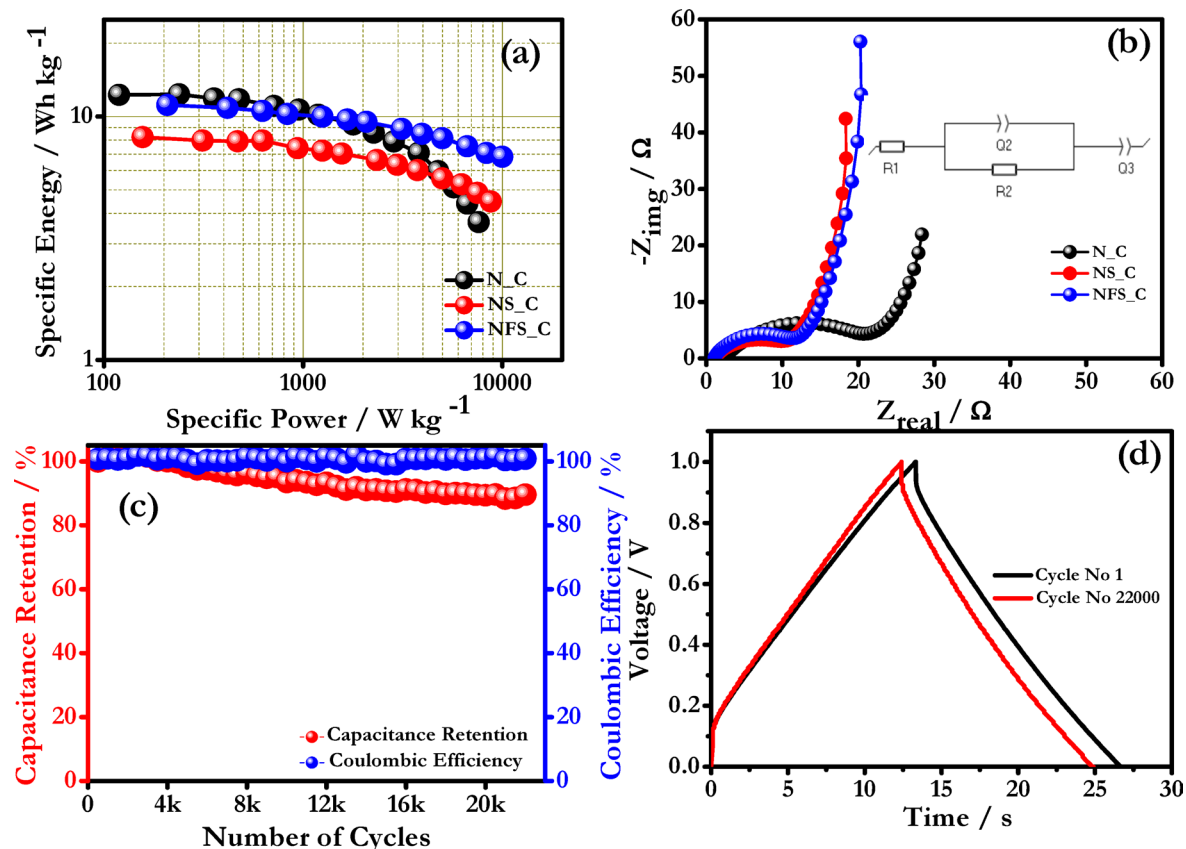


Fig. 9. **a** Ragone plot of the devices. **b** Nyquist plot comparing the impedance of the devices, **c** capacitance retention and coulombic efficiency plot for NSF_C sample. **d** Charging and discharging curves at 1st and 22,000th cycles.

Where E is the specific energy, P is the specific power, C_s is the specific capacitance, Δt is the discharge time, and V is the voltage window. N_C device delivers a specific energy of 12.26 Wh kg^{-1} at a power density of 119 W kg^{-1} but drops to 3.68 Wh kg^{-1} at a specific power of 7.6 kW kg^{-1} . Despite the lower value of specific energy (8.22 Wh kg^{-1}) at low specific power (156.25 W kg^{-1}), the NS_C device delivered a specific energy of 4.27 Wh kg^{-1} even at a higher specific power of 9.4 kW kg^{-1} . The NS_C device, unlike the N_C device, can retain specific energy over a broader range of specific power, indicating a better rate capability than the N_C device. The best performance in this regard is showcased by the NFS_C device, which delivers a high specific energy value of 11.15 Wh kg^{-1} at a specific power of 208 W kg^{-1} and a specific energy of 6.83 Wh kg^{-1} , even at a much higher specific power of 10 kW kg^{-1} . D. Zhu et al.⁴² report the synthesis and study of N-doped porous carbon spheres. The authors employed Schiff-base chemistry for the synthesis of the sample and investigated its application in supercapacitors. The material was reported to deliver a specific energy of 8.75 Wh kg^{-1} at a specific power of 500 W kg^{-1} . Lei Z et al.,⁴³ report the study and synthesis of mesoporous carbon spheres using silica spheres. In this work, the author demonstrates an approach to forming a carbon nanostructure where reduced graphene oxide sheets are intercalated within mesoporous carbon spheres. The symmetric device is reported to deliver a specific energy of 5.5 Wh kg^{-1} at a specific power of 50 W kg^{-1} . In this study, NFS_C SC is found to deliver better energy density than these works at wide range of rated current. It is also noted that the NFS_C device retains specific energy more effectively at high specific power, indicating versatility and superior rate capability compared to both N_C and NS_C devices, making it the most suitable device for high-energy and high-power applications. EIS was recorded for the fabricated samples from 100 kHz to 100 mHz at an amplitude of 10 mV . Figure 9b shows the Nyquist plot where the imaginary part and real part of the impedance are plotted to get information about the resistance and capacitance of the device. The equivalent circuit of the device is given in the inset. The semicircle part is the Nyquist plot is indicative of the capacitive behaviour of the devices and is due to the formation of the double layer at the electrode. The intercept on the real axis at the high-frequency region gives the solution resistance of the device. The linear spike towards 90° after the semicircle is characteristic of an EDLC device. The solution resistance (R_s) of the N_C, NS_C, and NFS_C devices is measured to be 2.46Ω , 1.26Ω , and 1.07Ω , respectively. The diameter of the semicircular part determines the charge transfer resistance (R_{ct}) of the device and was found to be 20 , 10.16 , and 9.74Ω for N_C, NS_C, and NFS_C, respectively. It can be concluded that the resistance is lower for devices fabricated with ternary-doped hollow carbon spheres. This reduction in resistance can be directly attributed to the doping of highly electronegative elements, such as F and S. The synergistic incorporation of nitrogen, sulfur, and fluorine dopants into the carbon matrix appears to enhance the electrical

conductivity of the material, as evidenced by electrochemical measurements. As shown in Fig. 7e, the cyclic voltammogram of the NFS_C-based device exhibits a nearly ideal rectangular shape, indicative of efficient capacitive behavior and low internal resistance. In contrast, the CV curve of the N_C sample (Fig. 7c) deviates more significantly from the rectangular profile, suggesting higher resistive losses. Similarly, Fig. 8b presents the GCD profiles of the samples for comparison. A pronounced IR drop is observed in the GCD curve of the N_C device, indicating significant internal resistance. In contrast, the GCD curve of the NFS_C device displays an almost ideal triangular shape with minimal IR drop, suggesting substantially reduced internal resistance. These observations are further corroborated by the EIS analysis, which confirms the reduced internal resistance in the NFS_C sample. To evaluate the device's performance over a large number of cycles, it was subjected to 22,000 cycles of continuous charging and discharging at a current density of 1 A g⁻¹. Kun-lin Liu et al.⁴⁴ report the synthesis of electrode material using Pitch-based porous aerogel composed of carbon onion nanospheres for EDLC applications. The material was reported to deliver a capacitance retention of 81.5% after 8000 cycles at 2 A g⁻¹. Jingjing Yan et al.⁴⁵ reported the synthesis and characterization of N/O-doped core-shell hierarchical porous carbon spheres for supercapacitor applications. The symmetric device fabricated is reported to deliver a capacitance retention of 86% up to only 10,000 cycles. Juan Dua et al.⁴⁶ reported the synthesis of hollow carbon spheres and dual-shell hollow carbon spheres using similar synthesis approaches. The dual-shell hollow carbon sphere sample was reported to exhibit better electrochemical performance and deliver a capacitance retention of 83.9% up to 10,000 cycles. Lei et al.⁴⁷ reported the synthesis of hollow carbon spheres with Polyaniline (PANI) deposited on their external surface. The work evaluates the electrocapacitive performance of the HCS-PANI composite with varying PANI content. The symmetric capacitor fabricated with the best sample is reported to deliver a capacitance retention of 73% after 1000 cycles. Bhattacharjya et al.⁴⁸ report the synthesis of Hollow mesoporous shell carbon capsules via a silica template method. The material is studied extensively for supercapacitor applications. The symmetric two-electrode device fabricated with the prepared material is reported to deliver a capacitance retention of 88% up to just 2000 charge-discharge cycles. Here, Fig. 9c shows the plot of capacitance retention percentage and coulombic efficiency against the number of cycles for the NFS_C device. The device was found to retain 89% of its initial capacitance and 100% coulombic efficiency after 22,000 cycles are given in Fig. 9c. This superior cyclic stability of the device could be attributed to the doping of the material with N, S, and F atoms, which has increased the structural stability of the material against high currents and a large number of charging and discharging cycles. The 1st and 22knd cycle of the GCD plot of NSF_C supercapacitor is given in Fig. 9d. It is clear from the Fig.9d that the device showing better stable performance over 22k cycle which is evidenced by the minimal deviation in the charge-discharge curve. The electrochemical performances of the existing supercapacitors have been given in the supporting information (Table ST1). Moreover, the post-cell analysis of the NFS_C symmetric supercapacitor has been carried out to understand the structural changes. The FE-SEM and elemental mapping analysis for the NFS_C||KOH||NFS_C symmetric supercapacitor have been carried out after 22k GCD cycles at 1 A g⁻¹ current density (Figure S4-negative electrode and Figure S5-positive electrode). It is clear that, even after 20,000 cycles, there is no change in the morphology of the sample. Still, a small agglomeration is visible due to the addition of PVDF and acetylene black during electrode preparation. The elemental mapping analysis depicts the presence of N, C, K, O, S, F, and Ni distributed throughout the sample for both positive and negative electrodes; the presence of potassium is from the KOH electrolyte used for the supercapacitor fabrication, as given in the supporting information, Figs. S4 and S5. Also, the NFS_C supercapacitor has been subjected to cycle life analysis for about 13,000 GCD cycles at 3 A g⁻¹ current density, to understand the device performance at high rated current. Initially, the capacitance retention percentage decreases, but after 3000 cycles, it gradually increases to 97% at 13,000 cycles, with a coulombic efficiency of nearly 99%, as shown in the supporting information (Fig. S6).

Conclusion

The investigation of heteroatom and ternary atom doping in hollow carbon spheres has led to the conclusion that the NFS_C device, despite the low specific surface area, exhibits superior performance when compared to the other two devices under study. This performance is attributed to the increased conductivity, pore size distribution and wettability of the co-doped material due to the presence of highly electronegative F and S. The NFS_C device also exhibits better high-rate capability than other devices investigated here. The NFS_C based capacitor device delivered a high specific energy value of 11.15 Wh kg⁻¹ at 208 W kg⁻¹ and retained a specific energy of 6.83 Wh kg⁻¹ even at higher specific power of 10 kW kg⁻¹. This makes NFS_C a better material for versatile and high-performance devices in a wide range of high-energy, high-power applications. The device fabricated using the ternary atoms doped sample exhibited excellent capacitance retention of 89% and coulombic efficiency of almost 100% up to 22,000 cycles at 1 A g⁻¹.

Data availability

Data is provided within the manuscript or supplementary information files.

Received: 15 April 2025; Accepted: 25 August 2025

Published online: 01 September 2025

References

1. Yadlapalli, R. T., Alla, R. K. R., Kandipati, R. & Kotapati, A. Super capacitors for energy storage: progress, applications and challenges. *J. Energy Storage*. **49** <https://doi.org/10.1016/j.est.2022.104194> (2022).
2. Navaneeth, P. et al. High surface area Cobalt aluminium layered double hydroxide printed electrodes for flexible supercapacitor and on-chip electrochemical bacterial lysing. *Electrochim. Acta*. **476** <https://doi.org/10.1016/j.electacta.2023.143744> (2024).

3. Mohanraj, M., Shaji, S. P., Rajni, K. S. & Ulaganathan, M. β -Ni(OH)₂/WC for high-energy aqueous hybrid supercapacitor. *Electrochim. Acta.* **482**, 143972. <https://doi.org/10.1016/j.electacta.2024.143972> (2024).
4. Shao, Y. et al. Design and mechanisms of asymmetric supercapacitors. *Chem. Rev.* **118**, 9233–9280. <https://doi.org/10.1021/acs.chemrev.8b00252> (2018).
5. You, X., Misra, M., Gregori, S. & Mohanty, A. K. Preparation of an electric double layer capacitor (EDLC) using miscanthus-derived biocarbon. *ACS Sustain. Chem. Eng.* **6**, 318–324. <https://doi.org/10.1021/acssuschemeng.7b02563> (2018).
6. Tian, Y. et al. Two-dimensional hexagonal-shaped mesoporous carbon sheets for supercapacitors. *ACS Omega.* **7**, 27896–27902. <https://doi.org/10.1021/acsomega.2c01149> (2022).
7. Prakash, H. C., Kumar, M. S., Lin, T. W. & Batabyal, S. K. Photo-assisted capacitive performance of V₂O₅ supercapacitor. *Electrochim. Acta.* **469** <https://doi.org/10.1016/j.electacta.2023.143229> (2023).
8. Liu, T., Zhang, L., Cheng, B. & Yu, J. Hollow carbon spheres and their hybrid nanomaterials in electrochemical energy storage. *Adv. Energy Mater.* **9** <https://doi.org/10.1002/aenm.201803900> (2019).
9. Yang, C. et al. Regulating solid electrolyte interphase film on fluorine-doped hard carbon anode for sodium-ion battery. *Carbon Energy.* **6** <https://doi.org/10.1002/cey2.503> (2024).
10. Mohapatra, D. et al. Sulfur doping: unique strategy to improve the supercapacitive performance of carbon nano-onions. *ACS Appl. Mater. Interfaces.* **11**, 8040–8050. <https://doi.org/10.1021/acsami.8b21534> (2019).
11. Saha, A., Paul, A., Srivastava, D. N. & Panda, A. B. Porous carbon incorporated B-Mo₂C Hollow sphere: an efficient electrocatalyst for hydrogen evolution reaction. *Int. J. Hydrogen Energy* 21655–21664. <https://doi.org/10.1016/j.ijhydene.2018.04.051> (2018).
12. Zheng, Y. et al. Template-free construction of Hollow mesoporous carbon spheres from a covalent triazine framework for enhanced oxygen electroreduction. *J. Colloid Interface Sci.* **608**, 3168–3177. <https://doi.org/10.1016/j.jcis.2021.11.048> (2022).
13. Verma, V., Choudhury, S. R., Rathour, V., Choudhury, S. R. & Ganesan, V. Hollow core mesoporous carbon spheres as catalyst support for improved platinum utilization in phosphoric acid fuel cells. *Microporous Mesoporous Mater.* **367** <https://doi.org/10.1016/j.micromeso.2024.113005> (2024).
14. Lou, Z. et al. Carbon sphere template derived Hollow nanostructure for photocatalysis and gas sensing. *Nanomaterials* **10** <https://doi.org/10.3390/nano10020378> (2020).
15. Lv, Y. et al. N/S co-doped coal-based porous carbon spheres as electrode materials for high performance supercapacitors. *RSC Adv.* **10**, 11033–11038. <https://doi.org/10.1039/d0ra00458h> (2020).
16. Zhang, K. et al. Nitrogen-doped porous interconnected double-shelled Hollow carbon spheres with high capacity for lithium ion batteries and sodium ion batteries. *Electrochim. Acta.* **155**, 174–182. <https://doi.org/10.1016/j.electacta.2014.12.108> (2015).
17. Sun, W., Zhang, Y. & Yang, F. Tuning electrochemical performance of carbon-sphere-based supercapacitors by compressive stress. *Electrochim. Acta.* **357** <https://doi.org/10.1016/j.electacta.2020.136874> (2020).
18. Feng, L. et al. Designing Hollow mesoporous carbon sphere for high-rate supercapacitor in water-in-salt electrolyte. *Chem. Eng. J.* **486** <https://doi.org/10.1016/j.cej.2024.150346> (2024).
19. Duraisamy, V. & Senthil Kumar, S. M. N and P dual heteroatom doped mesoporous Hollow carbon as an efficient oxygen reduction reaction catalyst in alkaline electrolyte. *Int. J. Hydrogen Energy.* **47**, 17992–18006. <https://doi.org/10.1016/j.ijhydene.2022.03.284> (2022).
20. To, J. W. F. et al. Ultrahigh surface area three-dimensional porous graphitic carbon from conjugated polymeric molecular framework. *ACS Cent. Sci.* **1**, 68–76. <https://doi.org/10.1021/acscentsci.5b00149> (2015).
21. Sajid, M., Chandio, Z. A., Hwang, B., Yun, T. G. & Cheong, J. Y. Graphitic carbon nitrides as electrode supporting materials for lithium-ion batteries: what Lies ahead in view of the current challenges? *Front. Energy Res.* **11** <https://doi.org/10.3389/feng.2023.1285044> (2023).
22. Xu, Y., Tan, R., Wu, J. & Huang, J. High-performance supercapacitors based on amorphous carbon derived from natural ramulus Mori. *Mater. Adv.* **3**, 6878–6886. <https://doi.org/10.1039/d2ma00426g> (2022).
23. Barranco, V. et al. Amorphous carbon nanofibers and their activated carbon nanofibers as supercapacitor electrodes. *J. Phys. Chem. C.* **114**, 10302–10307. <https://doi.org/10.1021/jp1021278> (2010).
24. Zólyomi, V., Koltai, J. & Kürti, J. Resonance Raman spectroscopy of graphite and graphene. *Phys. Status Solidi B Basic. Res.* **248**, 2435–2444. <https://doi.org/10.1002/pssb.201100295> (2011).
25. Xu, M. et al. Porous high specific surface area-activated carbon with co-doping N, S and P for high-performance supercapacitors. *RSC Adv.* **7**, 43780–43788. <https://doi.org/10.1039/c7ra07945a> (2017).
26. Dantas, S., Struckhoff, K. C., Thommes, M. & Neimark, A. V. Phase behavior and capillary condensation hysteresis of carbon dioxide in mesopores. *Langmuir* **35**, 11291–11298. <https://doi.org/10.1021/acs.langmuir.9b01748> (2019).
27. Sukhbaatar, B., Qing, W., Seo, J., Yoon, S. & Yoo, B. Uniformly dispersed ruthenium nanoparticles on porous carbon from coffee waste outperform platinum for hydrogen evolution reaction in alkaline media. *Sci. Rep.* **14** <https://doi.org/10.1038/s41598-024-56510-7> (2024).
28. Wang, Q. et al. Conversion of coal into N-doped porous carbon for high-performance SO₂ adsorption. *RSC Adv.* **12**, 20640–20648. <https://doi.org/10.1039/d2ra03098e> (2022).
29. Wang, J. et al. N-doped porous carbon derived from the pyrolysis of a Polydopamine-coated Hypercross-linked polymer for enhanced CO₂ adsorption. *Chem. Eur. J.* <https://doi.org/10.1002/chem.202402855> (2024).
30. Zhou, J. et al. Ultrahigh volumetric capacitance and Cyclic stability of fluorine and nitrogen co-doped carbon microspheres. *Nat. Commun.* **6** <https://doi.org/10.1038/ncomms9503> (2015).
31. Li, P. et al. Nitrogen and fluorine co-doped graphene for ultra-stable lithium metal anodes. *Nano Res.* **17**, 7212–7220. <https://doi.org/10.1007/s12274-024-6733-z> (2024).
32. Hu, J., Wang, Z., Chen, Y. & Xu, W. Fluorine-Doped graphene Oxide-Modified graphite felt cathode for hydrogen peroxide generation. *Catalysts* **14** <https://doi.org/10.3390/catal14110793> (2024).
33. Feng, L. L. et al. Metallic Co₉S₈ nanosheets grown on carbon cloth as efficient binder-free electrocatalysts for the hydrogen evolution reaction in neutral media. *J. Mater. Chem. Mater.* **4**, 6860–6867. <https://doi.org/10.1039/c5ta08611f> (2016).
34. Wang, T. et al. Recent advances in fluorine-doped/fluorinated carbon-based materials for supercapacitors. *Energy Storage Mater.* **30**, 367–384. <https://doi.org/10.1016/j.ensm.2020.04.044> (2020).
35. Du, J. et al. Micro/meso-porous Double-shell Hollow carbon spheres through spatially confined pyrolysis for supercapacitors and Zinc-ion capacitor. *Angew. Chem. Int. Ed.* <https://doi.org/10.1002/anie.202411066> (2024).
36. Noonan, O. et al. In situ Stöber templating: facile synthesis of Hollow mesoporous carbon spheres from silica-polymer composites for ultra-high level in-cavity adsorption. *J. Mater. Chem. Mater.* **4**, 9063–9071. <https://doi.org/10.1039/c6ta02265k> (2016).
37. Herde, Z. D., Dharmasena, R., Sumanasekera, G., Tumuluru, J. S. & Satyavolu, J. Impact of hydrolysis on surface area and energy storage applications of activated carbons produced from corn fiber and soy hulls. *Carbon Resour. Convers.* **3**, 19–28. <https://doi.org/10.1016/j.crcon.2019.12.002> (2020).
38. Czigány, Z. & Hultman, L. Interpretation of electron diffraction patterns from amorphous and fullerene-like carbon allotropes. *Ultramicroscopy* **110**, 815–819. <https://doi.org/10.1016/j.ultramic.2010.02.005> (2010).
39. Madeshwaran, M., Rajni, K. S. & Ulaganathan, M. Polyaniline@MoS₂: an organic and inorganic hybrid framework for asymmetric supercapacitor applications. *Mater. Today Chem.* **42** <https://doi.org/10.1016/j.mtchem.2024.102390> (2024).
40. Mishra, N. et al. MWCNTs synthesized from waste polypropylene plastics and its application in super-capacitors. *AIP Conf. Proc.* **228**–236. <https://doi.org/10.1063/1.4810063> (2013).

41. Markoulidis, F., Trapalis, C., Todorova, N., Grilli, R. & Lekakou, C. Composite electrodes of activated carbon and multiwall carbon nanotubes decorated with silver nanoparticles for high power energy storage. *J. Compos. Sci.* **3** <https://doi.org/10.3390/jcs3040097> (2019).
42. Zhu, D. et al. A general strategy to synthesize high-level N-doped porous carbons: via Schiff-base chemistry for supercapacitors. *J. Mater. Chem. Mater.* **6**, 12334–12343. <https://doi.org/10.1039/c8ta02341g> (2018).
43. Lei, Z., Christov, N. & Zhao, X. S. Intercalation of mesoporous carbon spheres between reduced graphene oxide sheets for Preparing high-rate supercapacitor electrodes. *Energy Environ. Sci.* **4**, 1866–1873. <https://doi.org/10.1039/c1ee01094h> (2011).
44. Lin Liu, K., Lun Jiao, M., Pan Chang, P., Yang Wang, C. & Ming Chen, M. Pitch-based porous aerogel composed of carbon onion nanospheres for electric double layer capacitors. *Carbon N Y.* **137**, 304–312. <https://doi.org/10.1016/j.carbon.2018.05.038> (2018).
45. Yan, J. et al. Core-shell hierarchical porous carbon spheres with N/O doping for efficient energy storage. *Electrochim. Acta.* **358** <https://doi.org/10.1016/j.electacta.2020.136899> (2020).
46. Du, J. et al. Rich porous dual-shell carbon spheres by dissolution-reassembly with high performance in supercapacitor. *J. Energy Storage.* **29** <https://doi.org/10.1016/j.est.2020.101375> (2020).
47. Lei, Z., Chen, Z. & Zhao, X. S. Growth of polyaniline on Hollow carbon spheres for enhancing electrocapacitance. *J. Phys. Chem. C.* **114**, 19867–19874. <https://doi.org/10.1021/jp1084026> (2010).
48. Bhattacharjya, D., Kim, M. S., Bae, T. S. & Yu, J. S. High performance supercapacitor prepared from Hollow mesoporous carbon capsules with hierarchical nanoarchitecture. *J. Power Sour.* **244**, 799–805. <https://doi.org/10.1016/j.jpowsour.2013.01.112> (2013).

Acknowledgements

M. U. acknowledges Amrita Vishwa Vidyapeetham for the financial support received through the AMRITA Seed Grant (Proposal ID: ASG2022069), and M.U. also acknowledges the financial support from the UGC-DAE CSR through a Collaborative Research Scheme (CRS) (project number: CRS/2022–23/04/898).

Author contributions

Sai Prem Shaji: Experiment, Fabrication of Devices, Data acquisition, testing analysis, Manuscript Writing; Madeshwara Mohanraj: Data collection, analysis, additional experiments during revision, manuscript editing. Author: Mani Ulaganathan: Problem design, Supervision, reviewing, editing, and resources.

Declarations

Competing interests

The authors declare no competing interests.

Additional information

Supplementary Information The online version contains supplementary material available at <https://doi.org/10.1038/s41598-025-17547-4>.

Correspondence and requests for materials should be addressed to U.M.

Reprints and permissions information is available at www.nature.com/reprints.

Publisher's note Springer Nature remains neutral with regard to jurisdictional claims in published maps and institutional affiliations.

Open Access This article is licensed under a Creative Commons Attribution-NonCommercial-NoDerivatives 4.0 International License, which permits any non-commercial use, sharing, distribution and reproduction in any medium or format, as long as you give appropriate credit to the original author(s) and the source, provide a link to the Creative Commons licence, and indicate if you modified the licensed material. You do not have permission under this licence to share adapted material derived from this article or parts of it. The images or other third party material in this article are included in the article's Creative Commons licence, unless indicated otherwise in a credit line to the material. If material is not included in the article's Creative Commons licence and your intended use is not permitted by statutory regulation or exceeds the permitted use, you will need to obtain permission directly from the copyright holder. To view a copy of this licence, visit <http://creativecommons.org/licenses/by-nc-nd/4.0/>.

© The Author(s) 2025